Supporting information for:

High Repetition Rate Optical Pump-Nuclear Resonance Probe Experiments Identify Transient Molecular Vibrations After Photoexcitation of a Spin Crossover Material

Sakshath Sadashivaiah[1,4,5], Juliusz A. Wolny[1], Lena Scherthan[1], Kevin Jenni[1], Andreas Omlor[1], Christina S. Müller[1], Ilya Sergueev[2], Marcus Herlitschke[2], Olaf Leupold[2], Hans-Christian Wille[2], Ralf Röhlsberger[2,3,4,5], and Volker Schünemann[1*].*

[1]Fachbereich Physik, Technische Universität Kaiserslautern, Erwin-Schrödinger Straße 46, 67663 Kaiserslautern, Germany.

[2] Deutsches Elektronen Synchrotron, Notkestraße 85, 22607 Hamburg, Germany.

[3] Friedrich-Schiller-Universität Jena, Max-Wien-Platz 1, 07743 Jena, Germany.

[4] Helmholtz-Institut Jena, Fröbelstieg 3, 07743 Jena, Germany.

[5] GSI Helmholtzzentrum für Schwerionenforschung GmbH, Planckstraße 1, 64291 Darmstadt, Germany.

1. Characterization of [Fe(PM-BiA)$_2$(NCS)$_2$] by scanning electron microscopy

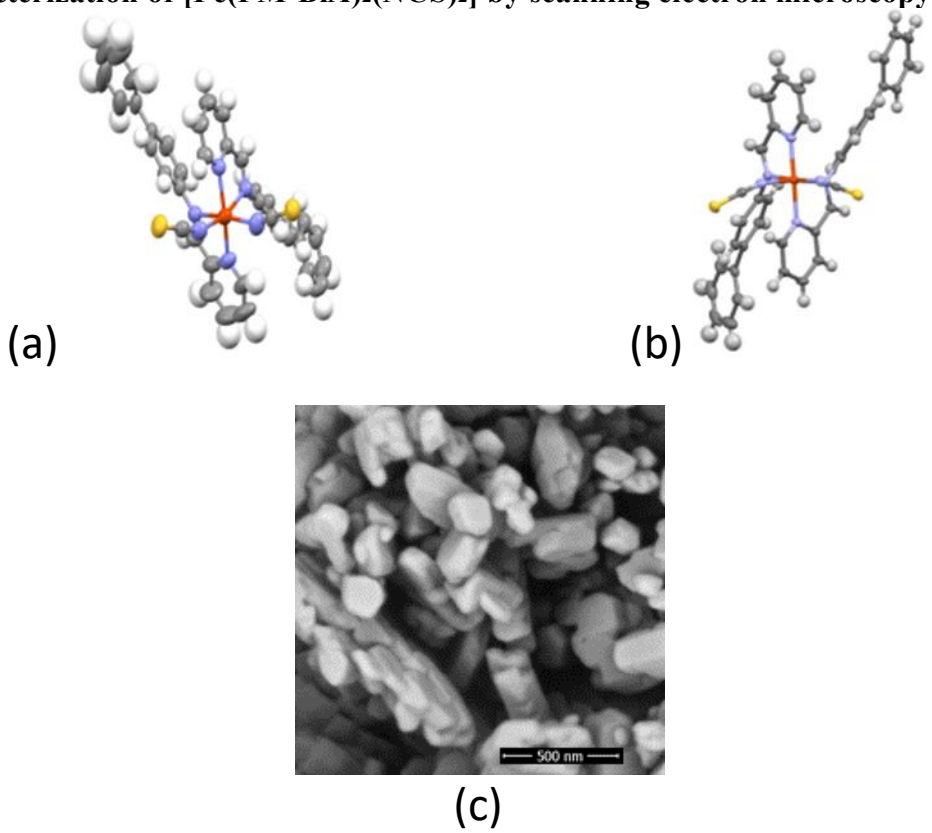

Figure S1. Molecular Structure corresponding to the (a) high spin state and (b) low spin state of the [Fe(PM-BiA)$_2$(NCS)$_2$] spin crossover complex **1**. (c) A scanning electron micrograph of the powder sample of the complex.

The mononuclear iron(II) containing spin crossover (SCO) complex [Fe(PM-BiA)$_2$(NCS)$_2$] denoted as **1** was prepared by established procedures, using ^{57}Fe [1]. The synthesis produces a polycrystalline mixture of two polymorphs, (I) with an orthorhombic structure and (II) with a monoclinic structure. Both polymorphs exhibit a first order phase transition from a low spin $t_{2g}^6e_g^0$ state (S=0) to high spin $t_{2g}^4e_g^2$ state (S=2). The transition of polymorph I is abrupt with a thermal hysteresis of 5K, while that of polymorph II is more gradual without an observable thermal hysteresis[2]. A scanning electron micrograph of the resulting powder is depicted in Figure

S1c. It shows the morphology of the surface of the powder sample. From the high-contrast image, we can deduce that the sample consists of crystalline nano-particles of an average size 200 nm.

2. Mössbauer spectroscopy and nuclear forward scattering

In order to determine the magnitude of the hyperfine interactions in the SCO complex **1**, conventional Mössbauer spectroscopy (MS) was performed. Representative data recorded at temperatures ranging from room temperature (RT) to 77 K are depicted in Figure S2a. The open symbols represent the data points. A pure high spin (HS) state is found at 298 K, whereas a mixture of low spin (LS) and HS components are found at lower temperatures. Using the Excel Macro VINDA[3] (thin absorber approximation), the spectra at each temperature are quantitatively analyzed by modelling them as a linear superposition of Lorentzian (doublet) line shapes caused by the absorption of gamma radiation by the individual components of the sample[3]. The simulated models are shown as continuous lines in Figure S2a. At 298 K a model with one Lorentzian doublet with a quadrupole splitting (ΔE_Q^{HS}) of 2.50 $\pm$ 0.02 mms^{-1} and an isomer shift (δ^{HS}) of 0.97 $\pm$ 0.02 mms^{-1} was sufficient to model the transmission data. These hyperfine parameters are characteristic of the HS (S=2) state of Fe(II) centers. At 220 K and 77 K, the appearance of an absorption in the spectrum at about 0.7 mms^{-1} indicates the emergence of the LS state and necessitates the inclusion of an additional component. At 220 K, the HS fraction (γ^{HS}) is 93.7 $\pm$ 0.02 %, while ΔE_Q^{HS} increases to 2.75 $\pm$ 0.03 mms^{-1} and δ^{HS} = 1.01 $\pm$ 0.03 mms^{-1}. The LS state comprises the remaining 6.3 $\pm$ 0.05 % with a quadrupole splitting (ΔE_Q^{LS}) of 0.63 $\pm$ 0.03 mms^{-1} and isomer shift (δ^{LS}) of 0.36 $\pm$ 0.02 mms^{-1}. At 77 K, γ^{HS} is very small (2.7 %) with ΔE_Q^{HS} = 3.05 $\pm$ 0.02 mms^{-1} and δ^{HS} = 1.12 $\pm$ 0.04 mms^{-1}, while most (97.3 %) of the sample has entered the LS state with ΔE_Q^{LS} = 0.65 $\pm$ 0.03 mms^{-1} and δ^{LS} = 0.41 $\pm$ 0.02 mms^{-1}. The non-zero, but small ΔE_Q^{LS} reflects the lower order of lattice symmetry than octahedral around the Fe atoms. We would like to point out that the transmission data in Figure S2a were also analyzed using transmission integrals using

the WINNORMOS software. The results were quantitively similar to those obtained using the thin absorber approximation in VINDA.

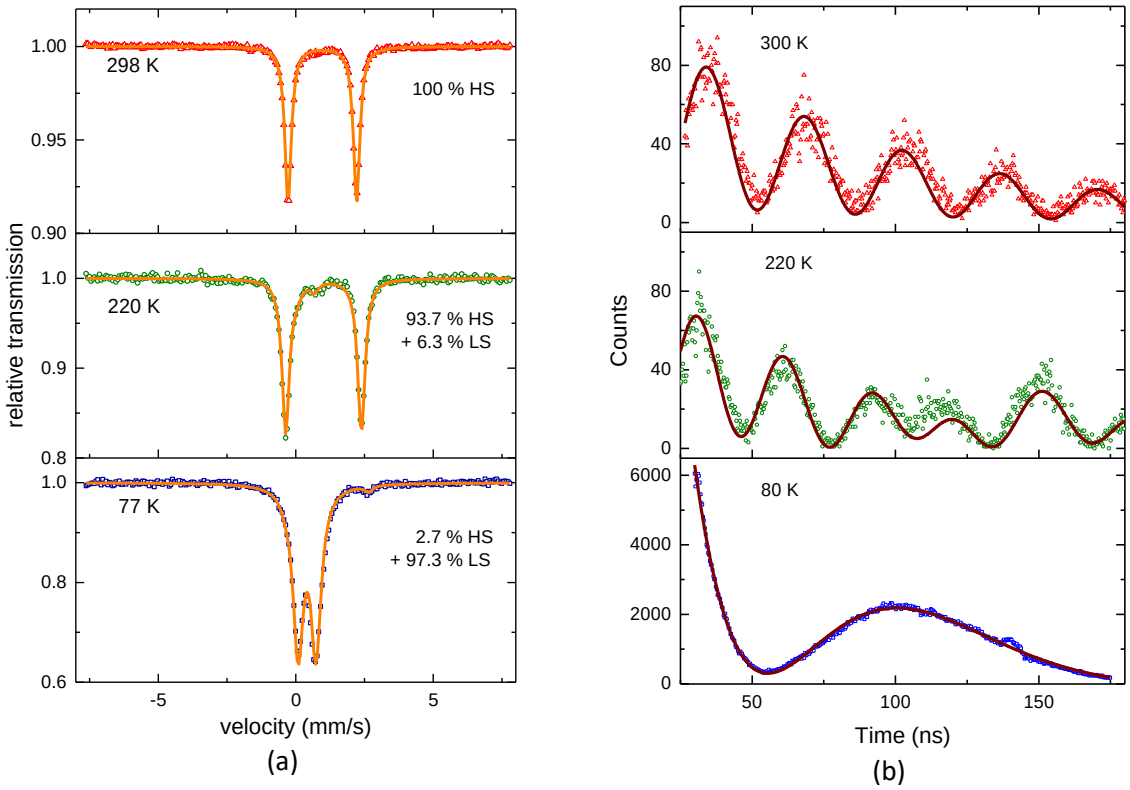

Figure S2. (a) Mössbauer spectra of **1** at 298 K, 220 K and 77 K. (b) The corresponding NFS spectra of the complex at 300 K, 220 K and 80 K. Parameters of the simulations (solid lines) are given in the text.

In order to compare the hyperfine parameters, as obtained by MS, we investigated the SCO complex **1** by nuclear forward scattering (NFS) using 14.412 keV synchrotron radiation (Pulse separation = 192 ns), at three different sample temperatures: 300 K, 220 K and 80 K. The data collected is depicted in Figure S2b as open symbols. The presence of a single regular beating pattern at 300 K and at 80 K indicates that the sample consists of mostly one spin-state at these two temperatures, while there is a mixture of two states at 220 K. The small disturbance in the data

at 138 ns is a result of a technical glitch during the experiment. The data is analyzed using a theoretical simulation of the forward scattering amplitudes, implemented in the CONUSS software, to extract the hyperfine parameters, the fraction of the sample excited to the HS state γ^{HS}, as well as the effective thickness t_{eff} of the samples [4]. The resulting simulations, depicted as continuous lines, show a good agreement with the experimental data. At 300 K, only one HS component was sufficient, indicating that the sample was entirely in the HS state. The simulations showed that ΔE_Q^{HS} = 2.52 $\pm$ 0.02 mms^{-1}, which is close to the value found using MS. At 220 K, analysis of the NFS data indicates that ΔE_Q^{HS} = 2.80 $\pm$ 0.02 mms^{-1}, δ^{HS} = 1.01 $\pm$ 0.02 mms^{-1}, ΔE_Q^{LS} = 0.63 $\pm$ 0.02 and δ^{LS} = 0.37 $\pm$ 0.02 mms^{-1}. These parameters are in good agreement with the hyperfine parameters obtained by MS. However, the NFS data indicates a presence of 25 $\pm$ 5 % LS state, which is slightly larger than that found by MS. At 80K, NFS data indicated that the sample is entirely in the LS state with ΔE_Q^{LS} = 0.59 $\pm$ 0.02 mms^{-1}, which is close to the value obtained by MS.

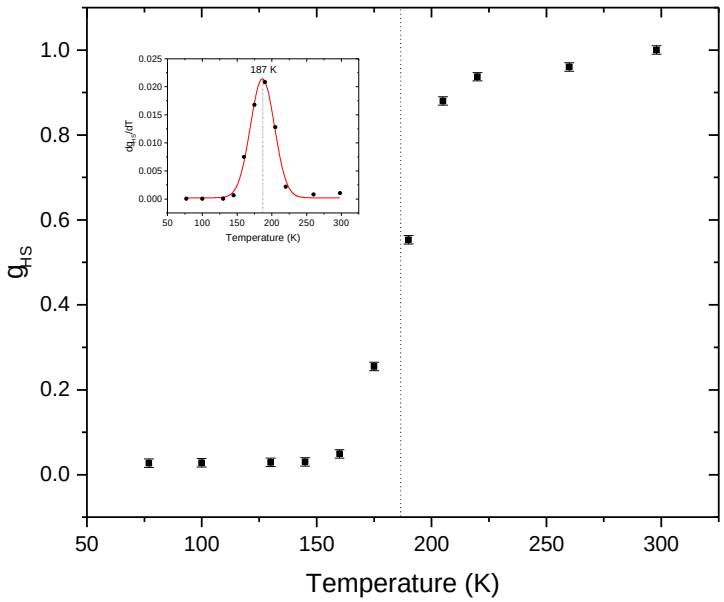

Figure S3. The variation of the HS fraction of **1** as determined by MS, showing the nature of the spin transition. The inset shows a differential curve to identify the transition temperature.

The nature of the spin transition for our polycrystalline sample can be illustrated by the change of γ^{HS} as a function of temperature. It is obtained by analyzing (using VINDA or WINNORMOS) the conventional MS data at various temperatures and is shown in figure S3. The transition is gradual, as in the monoclinic phase, with a transition temperature of $T_{1/2}$ = 187 K. Taking into account that reported values[2] of $T_{1/2}$ of the orthorhombic ($T_{½}\downarrow$ = 168K and $T_{½}\uparrow$ = 173 K) and the monoclinic ($T_{1/2}$ = 190K) phases of the complex under study we may assume that our sample consists of a mixture of both phases but corresponds predominantly to the monoclinic phase.

3. DFT simulation of an isolated molecule to model the pDOS obtained by nuclear inelastic scattering before laser-excitation

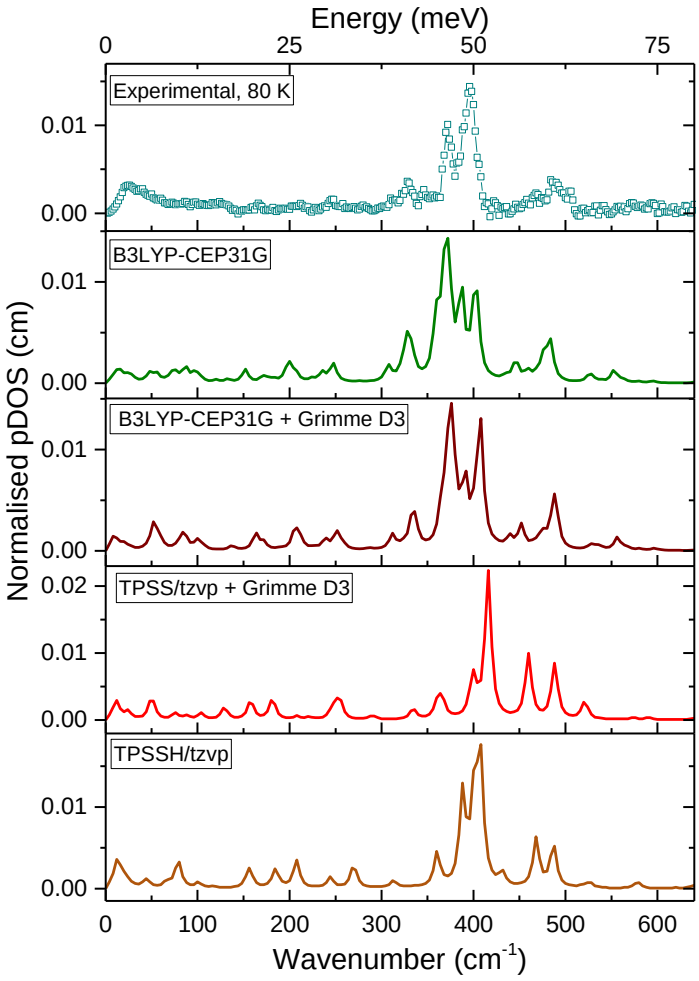

Figure S4. Experimental pDOS of complex **1** at 80 K and pDOS obtained via DFT simulations of the LS state using: B3LYP-CEP31G theory, B3LYP-CEP31G with Grimme D3 dispersion correction, TPSSh/tzvp and TPSS/tzvp + dispersion correction.

The four panels in Figure S4 show the pDOS of the LS predicted by DFT simulations. Generally, all four methods based on the optimisation of the geometry of a single molecule reproduce the characteristics of the experimental pDOS quite well. They differ qualitatively in predicted pattern of the intensive peaks observed in 360-410 cm^{-1} area. In the following part we will describe the

vibrational modes predicted using the B3LYP/CEP-31g + Grimme dispersion method in each region of the experimental pDOS. The first group of the observed band involves weak peaks, better seen at 4.2 K, between 528 and 595 cm^{-1}. In this area the simulations predict three vibrations (at 557, 530 and 527 cm^{-1}), corresponding to Fe-N_{imine} stretching, coupled either to C-H out of plane vibrations of biphenyl (see movie LS_557) or of pyridine ring (see movie LS_530). The second group of bands occurs in the 440-510 cm^{-1} region. The DFT calculations reveal seven vibrations in this area (at 489, 484, 482, 474, 466, 451, 440, and 437 cm^{-1}). The first three correspond to stretching (and some bending) of Fe-N_{NCS} and Fe-N_{py} bonds (see movies LS_489 and LS_482). The latter five involve the similar stretching, strong thiocyanate bending and pyridine (or bipy) out-of-plane bending (see movie LS_474). The third group of experimental vibrations are those of the most intense pDOS peaks in the region 360-420 cm^{-1}. The DFT simulation with the B3LYP/CEP-31g+dispersion approach predicts them to occur between 350 and 420 cm^{-1}. The strong peaks observed at 402, 396 and 377 cm^{-1} may be ascribed respectively to the vibrations predicted at 407, 401, 391, 380, 374, 368 and 365 cm^{-1}. The first four correspond to the stretching of all Fe-bonds (see movie LS_407), that at 374 cm^{-1} involves mainly Fe-py stretching (movie LS_374), the latter two mainly Fe-N_{imine} stretching, coupled to the C1-C1' diphenyl stretching. The fourth group observed in experiment involves the bands at 348, 333, 328, and 313 cm^{-1}. DFT calculation predict in this area four NIS-active vibrations at 337, 334, 323 and 312 cm^{-1}. They are due to modes involving Fe-N_{imine} and Fe-N_{py} stretching, coupled to the torsion and bending of the imine CHN fragment regarding the pyridine ring (see movie LS_337), the latter being part of the pyridine out-of-plane bending. The fifth group of observed bands are four, occurring at 282, 249, 213 and 165 cm^{-1}. The DFT calculations reveal nine vibrations at 258, 251, 239, 238, 212, 206, 205, 172 and 163 cm^{-1}, predominantly of N-Fe-N bending character (cf. movies LS_258 and

LS_172). Noteworthy are the observed vibrations at very low-frequencies, i.e. in the Debye region of the pDOS, which to the best of our knowledge have not been observed yet for the complex under study. They appear in the spectra of the powder sample at 35 and 39 cm^{-1} at 4.2 and 80 K, respectively. The DFT calculation for the single molecule predicts a vibration with significant Fe-amplitude in this area, particularly clearly for B3LYP/CEP-31g + dispersion and for TPSS/TZVP + dispersion. This mode, at 19 and 24 cm^{-1}, respectively, corresponds to the movement of the iron coupled to the butterfly-like movement of the ligands (see movie LS_19 and LS_tpss_disp_24).

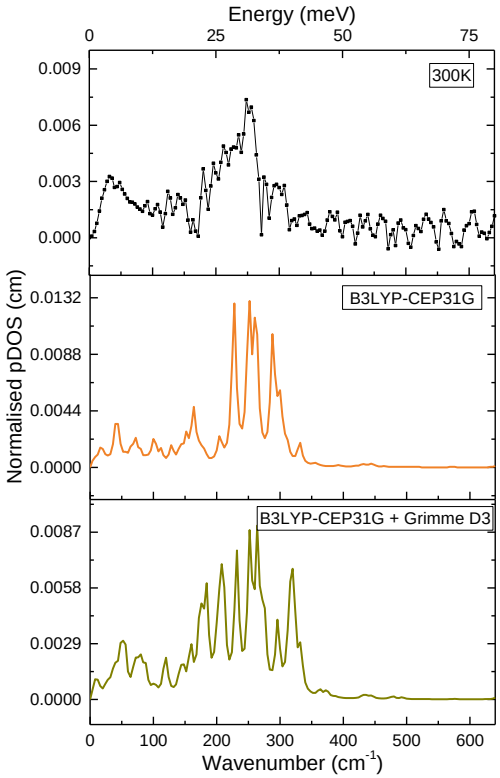

Figure S5. pDOS of **1** evaluated from experimental data (top panel) at 300 K, along with DFT simulations (the two lower panels) of the complex that depicts the HS state.

Figure S5 depicts the resulting pDOS upon heating the sample to 300 K, along with DFT simulations performed with and without the Grimme D3 frequency dispersion correction. The top panel shows the experimental pDOS, in which the softening of the metal-ligand vibrations is

evident in the appearance of phonon DOS in the range 170 – 320 cm^{-1} at 300 K. This is typical of the HS marker bands. Upon heating the powder sample to 300 K, the Fe-N bonding length increases from 1.976 Å in the low spin state (LS) to 2.171 Å (average values for B3LYP+dispersion calculations) in the high spin state. The lower 2 panels in Figure S5 show the pDOS predicted by DFT simulations. Again, we describe the vibrational modes predicted using only the B3LYP/CEP-31g + Grimme dispersion method. The double band with maxima at 312 and 298 cm^{-1} may be assigned to the Fe-N_{NCS} and Fe-N_{imine} stretching, coupled to the out-of-plane bending of the aromatic rings, predicted at 333, 322, 321, 315 and 296 cm^{-1} (cf. movies HS_333 and HS_296). The sharp band at 282 cm^{-1} may be assigned to the mode predicted at 274 cm^{-1} (see movie HS_274) revealing the Fe-N stretching with a high amplitude of the Fe- N_{NCS} stretching. The most characteristic feature of the spectrum of the high-spin isomer are two very intensive peaks at 259 and 250 cm^{-1} with several bands leading to a steep decrease down to ca. 170 cm^{-1}. The DFT simulations predict this band to be due to three modes with large amplitude vibrations of iron atom, occurring 264, 252 and 231 cm^{-1}. They involve the Fe-N stretching with pronounced amplitude of the Fe-N_{py} stretching (see movies HS_264 and HS_232). Furthermore, the band observed at 205 cm^{-1} may be assigned to three modes predicted at 210, 203 and 198, corresponding to Fe-N6 stretching (see movie HS_203). The next group of bands observed involves those at 154, 145 and 123 cm^{-1}. The DFT simulations yield the number of modes in this area, predominantly of bending character (see movie HS_159). In the Debye region of the experimental pDOS, a well-developed peak is observed at 49 cm^{-1} for the powder sample at 300 K. The DFT calculations reveal a number of modes at 30-60 cm^{-1} with that at 54 cm^{-1} showing a particularly large amplitude of vibration for the iron atom. Interestingly, this peak corresponds quite well to that predicted for the low-spin isomer at 19 cm^{-1} (see movie HS_54).

The bands observed in the experimental data (see Figure 1 of the main text) are well reproduced by the DFT simulations for the single molecules in the HS and LS states shown below the respective experimentally obtained data. However, there is a minor shift to lower energies in the simulated pDOS.

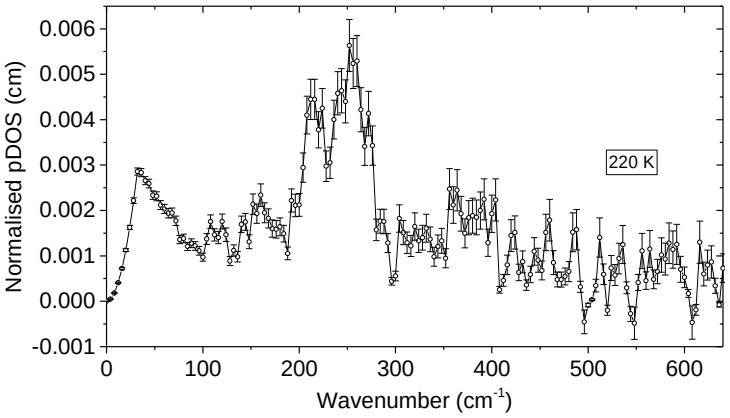

Figure S6. pDOS of **1** evaluated from the experimental data at 220 K, depicting a mixture of high spin and low spin states.

Figure S6 depicts the pDOS evaluated from the experimental NIS data of **1** at 220 K. Predominantly, the bands corresponding to the HS state are observed in the region up to 300 cm^{-1}, along with a small contribution from the LS state at higher wavenumbers. Using the *ina25* program, the Lamb- Mößbauer factor f can be evaluated along with other thermodynamic parameters [5].

Table S1. The temperature dependent Lamb-Mossbauer factors of **1**

T(K)	f_{exp} (for experimental data)	f_{sim} (for DFT simulations)
300	0.21 (±0.15)	0.03
220	0.45 (±0.15)	0.08

120	0.47 (±0.20)	0.32
80	0.55 (±0.05)	0.46

The *f*-factors determined from the experimental pDOS and the DFT simulations for temperatures from 80 K to 300 K are listed in Table S1. The values corresponding to simulations for 220 K and 120 K were estimated within the ina25 program using the simulation results of the HS and LS states respectively. It was found that the value of *f* was sensitive to small changes in experimental pDOS, which could lead to inaccuracies in the specification of the f-factor. Therefore, the calculation of the *f*-factor in this way necessitates a good signal to noise ratio in the NIS spectra. The *f*-factor increases with decreasing temperature with a sudden jump between 220 K and 120 K due to the spin-transition and because the f-factor of the LS state is higher than that of the HS state.

4. LIESST effect observed by conventional Mössbauer spectroscopy.

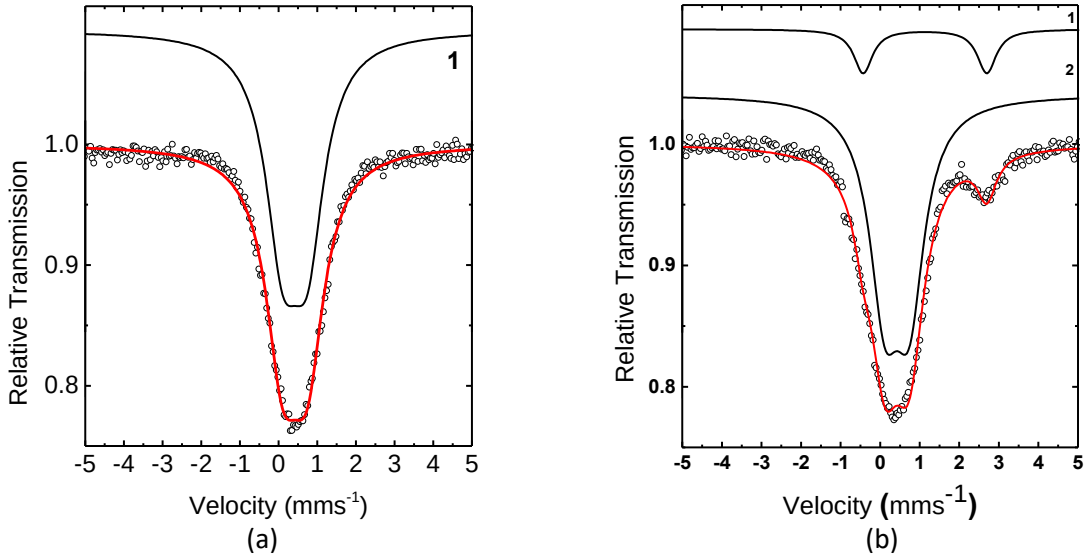

Figure S7. LIESST effect observed by irradiation with light of wavelength 766 nm and power 160 mW. (a) The Mössbauer spectrum of **1** before irradiation, at 4.2 K. (b) The Mössbauer spectrum after the irradiation for 1 hour.

The samples were also investigated for excitation by laser pulses in a MS experiment for the LIESST effect using the same laser that was used for our pump-probe experiment (see section 9.4 in this SI). Figure S7 shows the Mössbauer spectra obtained at 4.2 K before and after irradiating the sample with 766 nm laser light. The linewidth of absorption in the data is higher because of unavoidable vibrations of the closed-cycle cryostat. Without any light incident on the sample, the complex shows a typical Fe(II) LS spectrum with linewidth Γ= 1.07 mms^{-1}, δ^{LS} = 0.42 mms^{-1} and ΔE_Q^{LS} = 0.64 mms^{-1}. The complex was then irradiated for a period of 1 hour at a power level of 160 mW. The resulting spectra upon irradiation with 766 nm light is shown in Figure S7b. The spectra could be fitted with two Lorentzian doublet line shapes, one of which had the same quadrupole splitting as in the case with no light irradiation. The other component had Γ= 0.57 mms^{-1}, δ^{HS} =

1.13 mms^{-1} and ΔE_Q^{LS} = 3.12 mms^{-1}, which indicate a Fe(II) HS state. The hyperfine parameters of the NFS data and the MS data in the absence of light (Figure S2) are consistent with those in Figure S7. Similarly, a LIESST effect was also observed with 531 nm laser pulses (Figure S8). During the light irradiation, it was observed that the sample temperature rose by about 2.5 K in case of 766 nm and 4 K in case of 531 nm light pulses. The HS fraction created by the laser-excitation was about 6% in case of 531 nm and 25 % in case of 766 nm radiation. An increase of the duration of irradiation had no effect on the HS fraction created.

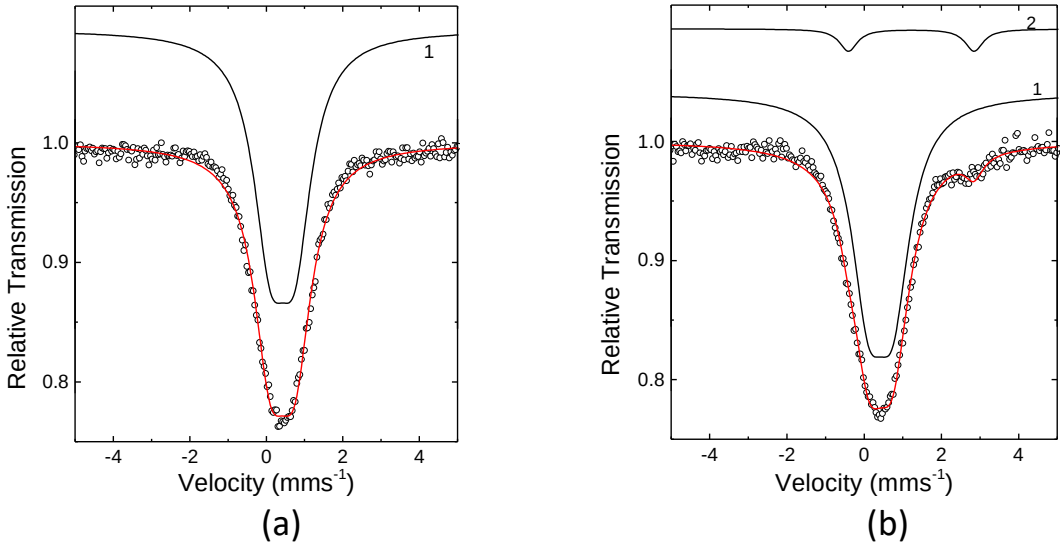

Figure S8. LIESST effect observed at 4.2 K by irradiation with light of wavelength 531 nm and power 160 mW. (a) The Mössbauer spectrum of **1** before irradiation, (b) The Mössbauer spectrum after the irradiation for 1 hour.

5. DFT simulations of a unit cell containing 4 molecules to model the experimental pDOS measured upon laser-excitation.

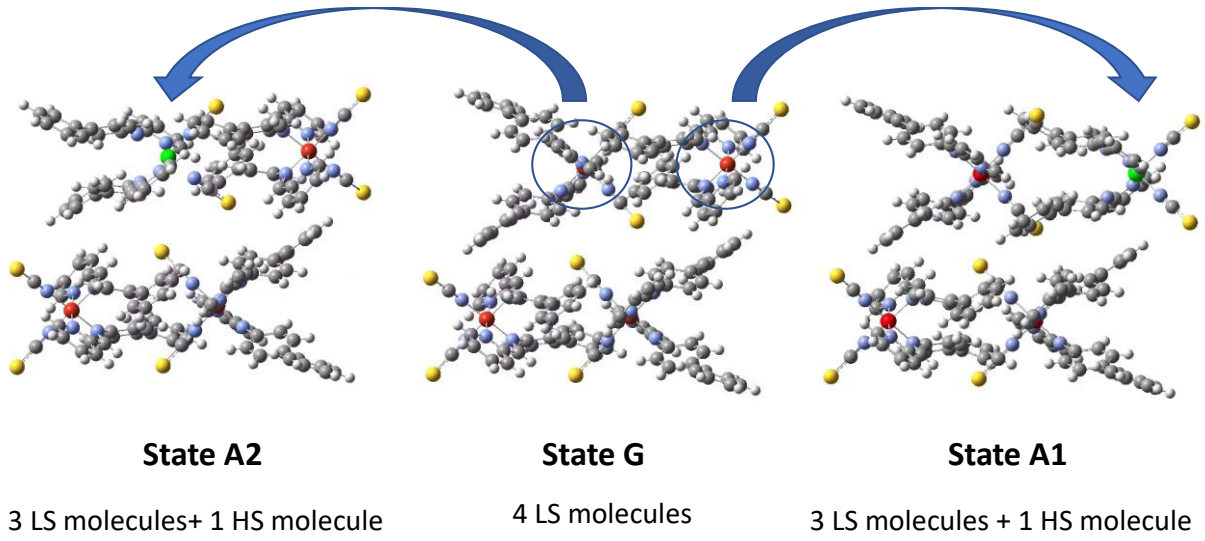

Figure S9. Schematic representation of the model used for DFT simulation of a unit cell of $[Fe(PM\text{-}BiA)_2(NCS)_2]$. State G is the ground state. Upon laser excitation, one of the 4 molecules is excited to a high spin sate. Model State A1: the unit cell content in which one low-spin isomer molecule was replaced with the equally located molecule of the high-spin cell. In this model the thiocyanate ligands of the high-spin "defect" point towards the biphenyl rings of the low-spin molecule in the same layer of the cell. This situation is reversed in the model for State A2.

It is important to discuss the relevancy of the applied model. Generally speaking, one can quite successfully reproduce the experimental results of the vibrational spectroscopy with the modeling of single molecules. On the other hand, the calculations of the vibrational pattern for the solid state of the larger molecules (based on the periodic boundary conditions approach) are hardly feasible because of the enormous demands of the computational time. Additionally, even when completed they reveal a limited accuracy, and a number of the imaginary frequencies are observed.[6,7] In a recent paper[8] Collet et al. presented periodic DFT calculations for the $Fe(phen)_2(NCS)_2$ system, revealing the results for the HS isomer. The calculated values of the N-CS stretching modes around

2100 cm^{-1} are typically shifted by 70-80 cm^{-1} regarding the experimental values. This accuracy is significantly lower than that obtained with modelling of single molecule. Still, in order to account for solid-state effects (i.e., the effects of the neighborhood of the LS and HS isomers) one has to model the crystal packing somehow. Our approach was to take the simplest model of the unit cell of the low-spin monoclinic phase and perform the frequency calculations for the non-optimized geometry of it and subsequently for this geometry in which one LS molecule was replaced with that of the HS one (taken also from the X-ray structure). We expected that to show a qualitative effect in the so calculated pDOS. Within this simplistic approach we model the observed effects of the 8% of HS spin defect with the system containing 25% of it. If we must extend the applied model in order into account for the LS to HS ratio of 8 %, we might have to take the content of the four unit cells, with sixteen molecules of, which one molecule would be the high-spin and model the ca. 6% HS material. Yet the computational demands would be much higher and the obtained improvement in the quality of fit need not be better.

In order to understand the active vibrations at the time delay of 1 ns, we performed DFT calculations, where the model consisted of not just an isolated molecule, but four molecules in a unit cell of the monoclinic polymorph with 3 molecules in the LS state and one occupying the corresponding position in the high-phase cell. The model of the unit cell is displayed in Figure S9. The results of the simulation are presented in Figure S10. In this way two different orientations of the high-spin molecule regarding the three low-spin ones were modelled. As mentioned before, the obtained results of frequency calculations yielded several imaginary frequencies. Yet, obtained pDOS patterns in optical phonon area are quite reasonable. Interestingly, the two models of 3:1 low-spin:high-spin cell content yield quite different pDOS pattern in the 180-350 cm^{-1} region. While both models predict two bands with maxima at ca. 270 and 290 cm^{-1} (observed in difference

spectrum) only the state A2 results in reproduction of the bands seen in difference spectrum at ca. 230 and 340 cm^{-1} (with a weaker one at ca. 320 cm^{-1}). The first two are apparently due to the vibrations of the high-spin molecules. That predicted at 289 cm^{-1} corresponds to the Fe-N_{py} stretching coupled to the out-of-plane bending of the pyridine ring (see movie sub3_289), while that at 268 cm^{-1} (see movie sub3_268) to Fe-N stretching involving the pyridine and thiocyanate ligands. On the other hand, the bands predicted only with the model of state A2 are due to vibrations of the high-spin and low-spin molecules. That at ca. 230 cm^{-1} is again due to high-spin Fe-N stretching, coupled with some bending of the low-spin molecule in the same layer. The band predicted at ca. 340 cm^{-1} (see movie sub3_337) involves a combination of stretching and bending of Fe-N bonds of the low-spin molecule. Interestingly, the latter mode is not predicted by the simulations for four low-spin molecules in the unit cell, although the calculations for the isolated low-spin complex display a band in this region (see Figure 1, main text). Also, the calculations display several vibrations in the 15-40- cm^{-1} region, similar to those seen in experiment.

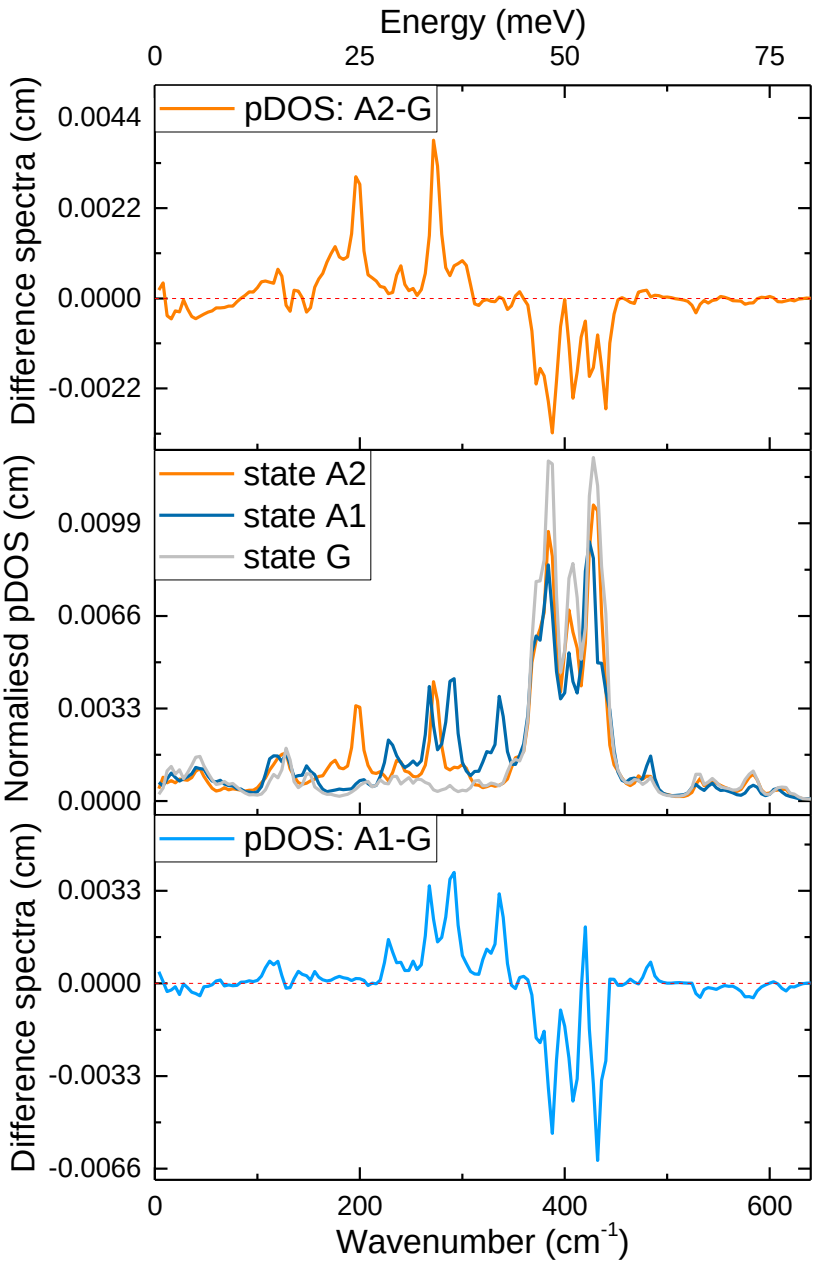

Figure S10. The simulated pDOS of a unit cell containing 4 molecules of $[Fe(PM\text{-}BiA)_2(NCS)_2]$. (see the models shown in Figure S9).

6. NIS characterization of $[Fe_{0.9}Zn_{0.1}(PM\text{-}BiA)_2(NCS)_2]$

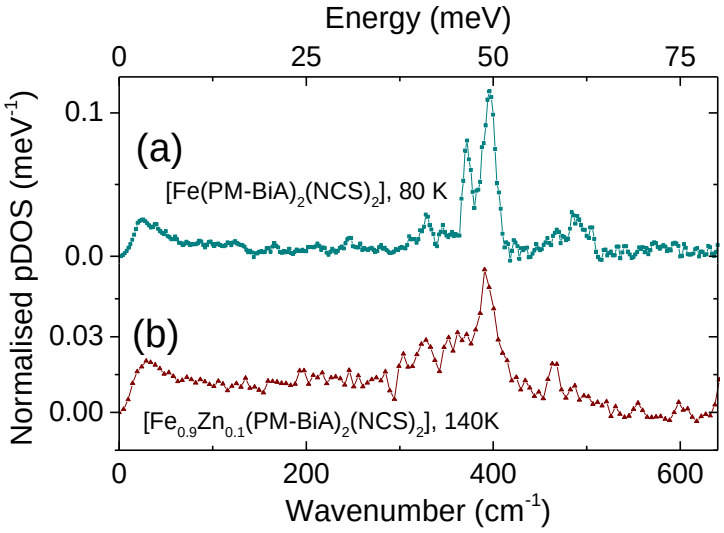

Figure S11. (a) pDOS of **1** at 80K, compared with (b) pDOS of **2** at 140K.

When Fe(II) spin crossover complexes are doped with Zn^{2+} at the iron sites, they mimic the behavior of a high spin molecule because Zn^{2+} is isostructural with Fe(II) high spin. Figure S11 shows the Fe-projected pDOS of $[^{57}Fe_{0.9}Zn_{0.1}(PM\text{-}BiA)_2(NCS)_2]$ denoted as **2**, as compared with that of $[^{57}Fe(PM\text{-}BiA)_2(NCS)_2]$ denoted as **1**. There is a clear difference in the pattern of the low spin phase, indicating that the vibration of the Fe-centers in **2** is different from the low spin state of **1**.

7. Mössbauer spectroscopy of $[Fe_{0.9}Zn_{0.1}(PM\text{-}BiA)_2(NCS)_2]$

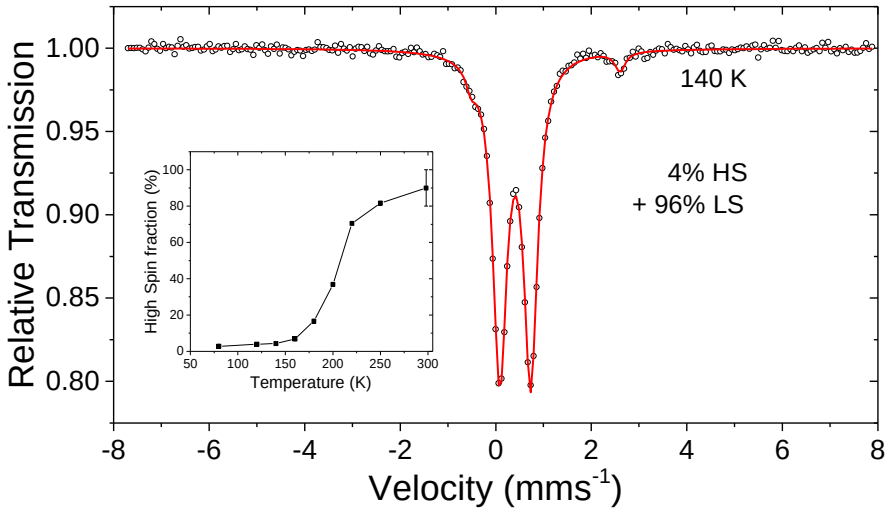

Figure S12. Mössbauer spectrum of **2** at 140 K. The inset shows the high spin fraction as a function of temperature.

A Mössbauer spectrum obtained at 140 K of **2** is shown in Figure S12. The open spheres are the data points indicating a mixture of a predominant low spin component, along with a small contribution from a high spin state. The continuous line shows the simulated model with two Lorentzian doublets with 96 ± 1 % low spin and 4 ±1 % high spin. The respective quadrupole splittings of the doublets are 0.65 ± 0.02 mms^{-1} and 3.11 ± 0.02 mms^{-1}. The respective isomer shift values are 0.41 ± 0.02 mms^{-1} and 1.05 ± 0.02 mms^{-1}. The inset shows the variation of the high spin fraction of **2** as the temperature is lowered from room temperature to 80 K, which indicates the transition from the high spin to the low spin state. These data sets indicate that at 140 K, the material is mostly in the low spin Fe(II) state.

8. NIS raw data for pump-probe measurements

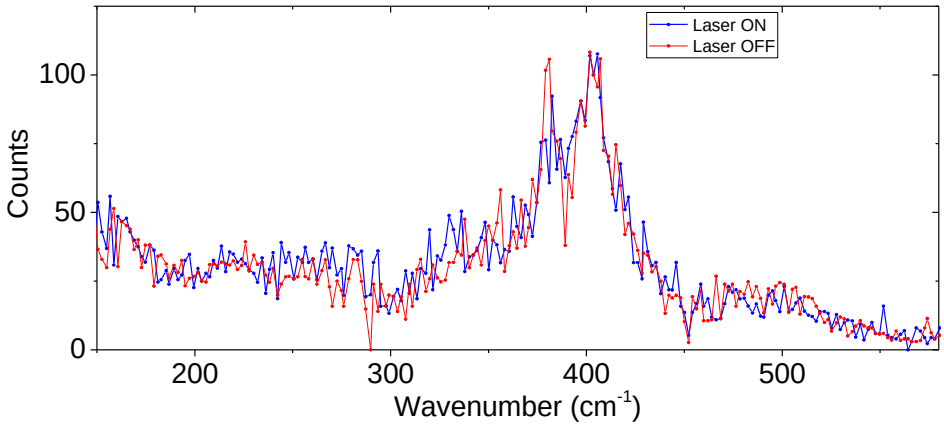

Figure S13. NIS spectrum (raw data) for the laser-ON and laser-OFF cases.

To substantiate the differences in the pDOS of the ground state and excited state of **1** (referred to as Laser off and Laser on data in Figure 3 of the main manuscript), the averaged NIS spectrum is shown in Figure S13. The differences seen in the experimental pDOS in Figure 3a can also be seen in the counts of the NIS spectrum in the corresponding bands in Figure S13.

9. Experimental details and methods

9.1 Scanning electron microscopy

Scanning electron microscopy was performed using a Helios Nanolab 650 microscope manufactured by FEI. We used a semiconducting detector for imaging using secondary backscattered electrons in order to get a high contrast image of the nanocrystals. The nanocrystals in the powder form were attached to an aluminium stub using silver glue and subsequently sputter-coated with 15 nm Ir (invisible in the electron micrograph) to avoid charging of the nanocrystals during imaging.

9.2 Mössbauer spectroscopy and LIESST

Mössbauer spectra were recorded in transmission geometry using a spectrometer from WissEl GmbH, operated in the constant acceleration mode with 512 channels and a maximum velocity of about 8 mms^{-1}. Isomer shifts are relative to a 25 μm thick α-Fe foil, which was used for velocity calibration at room temperature. The detector consisted of a proportional counter and the source contained ^{57}Co diffused in Rh with an activity of 0.4 GBq. For temperature control from 77 K up to room temperature, samples were placed in a continuous flow cryostat (OptistatDN, Oxford Instruments). Spectral data were analyzed using the public domain program VINDA running on an Excel 2003© platform. The spectra were analyzed by least squares fits using Lorentzian line shapes. The experimental errors with respect to the reported isomer shifts, quadrupole splittings and line widths are ~ ± 0.03 mms^{-1}. The experimental error for the relative area is ~ ± 1 %.

For the LIESST experiments, a similar spectrometer was used but the samples were placed in a closed cycle cryostat (Cryo Industries of America Inc.), which has an optical window along the direction perpendicular to the movement of the ^{57}Co source. To study the light-induced effect, the

samples were rotated towards the optical window and irradiated with the same laser system that was used in the pump-probe experiments at the synchrotron (see section 9.4) before rotating them back for Mössbauer spectroscopy.

9.3 Nuclear resonance scattering

Nuclear resonance scattering (NFS and NIS) was performed at the Dynamics beamline P01, PETRA III, DESY, Hamburg. The synchrotron was operated in a 40-bunch mode. The corresponding time interval between adjacent synchrotron radiation (SR) pulses is 192 ns, which is sufficient to measure the ^{57}Fe nuclear transition and suited for pump-probe measurements. The SR pulses were monochromatized using a high heat load monochromator and a high-resolution monochromator to a bandwidth of approximately 1 meV. Subsequently, the SR beam was focused to a size of 500 μm × 200 μm at the sample position. A silicon avalanche photodiode (APD), placed 1.5 m from the sample position, was used to detect the NFS spectra. Another APD covered by a black Kapton foil was placed close to the sample position to detect the NIS spectra. For the measurements between 80 K and 300 K, we use a liquid nitrogen cryostream manufactured by Oxford Cryosystems. For the 4.2 K measurement, the sample was mounted in a liquid helium cryostat manufactured by Janis Research.

9.4 Pump-probe measurements

Optical excitation was caused by a 531 nm pulsed laser source (pulse width <100 ps) manufactured by Picoquant GmbH, Berlin. The laser beam had an energy of 2.5 nJ per pulse. The laser head was externally triggered to fire at half the repetition rate of the SR pulses, using clock pulses that are generated by electronically delaying the synchrotron bunch clock signal. The timing

of the laser pulses was adjusted as described in [9]. The time resolution is ± 0.3 ns (although, it is technically limited only by the pulse width of the synchrotron pulses since the laser pulse width can even be in the fs-regime) due to this method of delaying the laser pulses by electronically delayed clock pulses. The laser beam was guided using mirrors and focused to a spot slightly larger than 600 μm in diameter at the sample position. The probe, consisting of synchrotron pulses, was focused using Be lenses to a size smaller than 200 μm. The sample was mounted at the tip of a Graphite rod using high vacuum grease and its temperature was controlled using a liquid nitrogen cryostream manufactured by Oxford Cryosystems.

9.5 Density functional theory calculations

The density functional theory calculations were performed using Gaussian 16, Revision A.03 [10] implemented on the high performance computer cluster Elwetritsch II of the RHRK at TU Kaiserslautern. The normal vibrations analysis was performed for the high-spin and low-spin isomers of the title compound. For both optimization and frequency calculations the B3LYP-CEP31G theory was applied for an isolated molecule. Additionally, the same combination of the exchange-correlation/basis set was applied, including the Grimme D3 dispersion correction. For the low-spin isomer, further calculations involving TPSSh/tzvp and TPSS/tzvp + dispersion correction were performed in order to test the quality of the reproduction of the experimentally obtained pDOS. Finally, the frequency calculation for the four low-spin molecules basing on the crystal structure of the monoclinic polymorph was performed, using the non-optimized coordinates corresponding to the four molecules in the unit cell of the polymorph. The latter approach obviously resulted in numerous imaginary frequencies but was useful for the qualitative analysis of the NIS spectra obtained upon irradiation by laser pulses.

REFERENCES

(1) Létard, J.-F.; Guionneau, P.; Rabardel, L.; Howard, J. A. K.; Goeta, A. E.; Chasseau, D.; Kahn, O. Structural, Magnetic, and Photomagnetic Studies of a Mononuclear Iron(II) Derivative Exhibiting an Exceptionally Abrupt Spin Transition. Light-Induced Thermal Hysteresis Phenomenon. *Inorg Chem* **1998**, *37* (17), 4432–4441.

(2) Létard, J.-F.; Chastanet, G.; Nguyen, O.; Marcén, S.; Marchivie, M.; Guionneau, P.; Chasseau, D.; Gütlich, P. Spin Crossover Properties of the [$Fe(PM\text{-}BiA)_2(NCS)_2$] Complex - Phases I and II. *Monatshefte fur Chemie* **2003**, *134* (2), 165–182.

(3) Gunnlaugsson, H. P. Spreadsheet Based Analysis of Mössbauer Spectra. *Hyperfine Interact.* **2016**, *237* (1), 79.

(4) Sturhahn, W. CONUSS and PHOENIX: Evaluation of Nuclear Resonant Scattering Data. *Hyperfine Interact.* **2000**, *125* (1), 149–172.

(5) Kohn, V. G.; Chumakov, A. I. DOS: Evaluation of Phonon Density of States from Nuclear Resonant Inelastic Absorption. *Hyperfine Interact.* **2000**, *125* (1–4), 205–221.

(6) Paulsen, H.; Schünemann, V.; Wolny, J. A. Progress in Electronic Structure Calculations on Spin-Crossover Complexes. *Eur. J. Inorg. Chem.* **2013**, *2013* (5-6), 628–641.

(7) Wolny, J. A.; Diller, R.; Schünemann, V. Vibrational Spectroscopy of Mono- and Polynuclear Spin-Crossover Systems. *Eur. J. Inorg. Chem.* **2012**, *2012* (16), 2635–2648.

(8) Collet, E.; Azzolina, G.; Ichii, T.; Guerin, L.; Bertoni, R.; Moréac, A.; Cammarata, M.; Daro, N.; Chastanet, G.; Kubicki, J.; Tanaka, K.; Matar, S. F. Lattice Phonon Modes of the Spin Crossover Crystal [$Fe(Phen)_2(NCS)_2$] Studied by THz, IR, Raman Spectroscopies and DFT Calculations. *Eur. Phys. J. B* **2019**, *92* (1), 12.

(9) Sakshath, S.; Jenni, K.; Scherthan, L.; Würtz, P.; Herlitschke, M.; Sergeev, I.; Strohm, C.; Wille, H.-C.; Röhlsberger, R.; Wolny, J. A.; Schünemann, V. Optical Pump - Nuclear

Resonance Probe Experiments on Spin Crossover Complexes. *Hyperfine Interact.* **2017**, *238* (1), 89.

(10) Frisch, M. J.; Trucks, G. W.; Schlegel, H. B.; Scuseria, G. E.; Robb, M. A.; Cheeseman, J. R.; Scalmani, G.; Barone, V.; Petersson, G. A.; Nakatsuji, H.; Li, X.; Caricato, M.; Marenich, A. V; Bloino, J.; Janesko, B. G.; Gomperts, R.; Mennucci, B.; Hratchian, H. P.; Ortiz, J. V; Izmaylov, A. F.; Sonnenberg, J. L.; Williams-Young, D.; Ding, F.; Lipparini, F.; Egidi, F.; Goings, J.; Peng, B.; Petrone, A.; Henderson, T.; Ranasinghe, D.; Zakrzewski, V. G.; Gao, J.; Rega, N.; Zheng, G.; Liang, W.; Hada, M.; Ehara, M.; Toyota, K.; Fukuda, R.; Hasegawa, J.; Ishida, M.; Nakajima, T.; Honda, Y.; Kitao, O.; Nakai, H.; Vreven, T.; Throssell, K.; Montgomery Jr., J. A.; Peralta, J. E.; Ogliaro, F.; Bearpark, M. J.; Heyd, J. J.; Brothers, E. N.; Kudin, K. N.; Staroverov, V. N.; Keith, T. A.; Kobayashi, R.; Normand, J.; Raghavachari, K.; Rendell, A. P.; Burant, J. C.; Iyengar, S. S.; Tomasi, J.; Cossi, M.; Millam, J. M.; Klene, M.; Adamo, C.; Cammi, R.; Ochterski, J. W.; Martin, R. L.; Morokuma, K.; Farkas, O.; Foresman, J. B.; Fox, D. J. Gaussian 16 Revision A.03. 2016.